Journal of Power Sources 212 (2012) 28–34

Contents lists available at SciVerse ScienceDirect

Journal of Power Sources

journal homepage: www.elsevier.com/locate/jpowsour

Ultrafine $LiMn_2O_4$/carbon nanotube nanocomposite with excellent rate capability and cycling stability for lithium-ion batteries

Hui Xia [a,*], Krishna Rao Ragavendran [b], Jianping Xie [c], Li Lu [d]

[a] School of Materials Science and Engineering, Nanjing University of Science and Technology, Xiaolingwei 200, Nanjing, Jiangsu 210094, China
[b] Department of Chemistry, Bar-Ilan University, Ramat-Gan 52900, Israel
[c] Department of Chemical and Biomolecular Engineering, National University of Singapore, 9 Engineering Drive 1, Singapore 117576, Singapore
[d] Department of Mechanical Engineering, National University of Singapore, 9 Engineering Drive 1, Singapore 117576, Singapore

ARTICLE INFO

Article history:
Received 21 January 2012
Received in revised form
13 March 2012
Accepted 15 March 2012
Available online 9 April 2012

Keywords:
Lithium-ion batteries
Cathode
Lithium manganese oxide
Carbon nanotube
Nanocomposite

ABSTRACT

Ultrafine $LiMn_2O_4$/carbon nanotube (CNT) nanocomposite is synthesized by a one-step hydrothermal treatment. In the nanocomposite, $LiMn_2O_4$ nanoparticles of 10-20 nm in diameters are well crystallized and uniformly distributed in the CNT matrix. The CNTs not only provide a conductive matrix, facilitating fast electron transport, but also effectively reduce agglomeration of $LiMn_2O_4$ nanoparticles. The nano-$LiMn_2O_4$/CNT nanocomposite exhibits superior rate capability and cycling stability compared with the sol-gel synthesized $LiMn_2O_4$, making it promising for high-power applications.

1. Introduction

Recently, lithium-ion batteries have attracted a lot of research interest due to their potential applications in hybrid electric vehicles (HEV) and full electric vehicles (EV) [1-3]. Although lithium-ion batteries can provide higher energy density than other secondary battery systems, their power density remains too low for high power applications such as HEV and EV. Power density can be improved by a suitable choice of positive and negative electrode materials leading to a higher voltage and to higher charge/discharge rates. In general, lithium transition metal oxides with higher working voltages vs. lithium are often selected as positive electrode materials for lithium-ion batteries [4]. There are generally two methods to increase the charge/discharge rates. One method is to reduce the crystallite size of the electrode materials, which as a consequence of shortened electron and lithium ion diffusion paths [5] lead to enhanced charge/discharge rates. Another method is to add conductive additives to the electrode materials to make composites, which could enhance the charge/discharge rates due to the improved electronic conductivity of the electrode [5, 6].

Commercial lithium-ion batteries often employ layered $LiCoO_2$ as the cathode material. However, low thermal stability and high cost of $LiCoO_2$ shifted the research efforts towards the search for alternative cathode materials [7]. Replacing $LiCoO_2$ with $LiMn_2O_4$ leads to a higher electrochemical potential vs. graphite, a better safety and lower production cost. These virtues of $LiMn_2O_4$ have attracted researchers and a lot of efforts have been devoted to developing nanostructured $LiMn_2O_4$ and carbon/$LiMn_2O_4$ composite, aiming at improving the power capability and cycling stability to fulfill the high power requirements of HEV and EV [8-12]. Various nanostructures of $LiMn_2O_4$, such as nanoparticles [13], nanowires [14], nanorods [15], nanotubes [16], and nanoporous structures [17], have been developed and their electrochemical properties have been reported. However, the synthesis of these nanostructures of $LiMn_2O_4$ usually includes complex and multi-step procedures [18], which may be difficult to be employed for mass-production and commercialization. For example, $LiMn_2O_4$ nanowires were reported to be synthesized by a two-step approach [18]. First MnO_2 nanowires were prepared by a solvothermal reaction. In the successive step, $LiMn_2O_4$ phase was obtained by solid state reaction between the prepared MnO_2 nanowrie and LiOH at low pressure in oxygen atmosphere. Since the cost of cathode material depends on the nature of synthesis, it is imperative to develop simple synthesis methods with cheap reagents and low synthesis temperatures.

* Corresponding author. Tel.: +86 25 84315606; fax: +86 25 84315159.
E-mail addresses: jasonxiahui@gmail.com, xiahui@njust.edu.cn (H. Xia).

0378-7753/$ – see front matter © 2012 Elsevier B.V. All rights reserved.
doi:10.1016/j.jpowsour.2012.03.079

Carbon/$LiMn_2O_4$ composites have also been reported by several groups [19, 20]. However, the synthesis involved multi-step procedures, consuming several days [20]. Furthermore, the particle size of the synthesized material was not small enough to achieve the required high power capability.

In this work, we report a direct one-step synthesis of ultrafine $LiMn_2O_4$/CNT nanocomposite by a hydrothermal treatment within 5 h. The particle size of $LiMn_2O_4$ in the nanocomposite was found to be in the range of 10 - 20 nm. The CNTs serve as both conductive matrix and blockers, not only facilitating fast electron transport but also reducing the agglomeration of nanocrystalline $LiMn_2O_4$ particles. The ultrafine $LiMn_2O_4$/CNT nanocomposite exhibits excellent electrochemical performance in terms of high rate capability and cycling stability.

2. Experimental

2.1. Synthesis

A one-step hydrothermal treatment was used to synthesize the ultrafine $LiMn_2O_4$/CNT nanocomposite. Multiwalled CNTs (20 ~ 50 nm in diameter, Shenzhen Nanotech Port Co., Ltd.) were purified by refluxing the as-received sample in 10 wt% nitric acid for 12 h. All the other chemicals employed were of analytical grade and were used directly without any further purification. In the typical process, 0.05 g CNTs were dispersed in 25 cm^3 deionized (DI) water by ultrasonic vibration for 2 h. 0.3 g $KMnO_4$ was then added in the above suspension and the mixed solution was stirred by a magnetic bar for 1 h. In the next step, 0.08 g LiOH and 1 cm^3 ethanol were added in the solution and the solution was further stirred for another 1 h. Finally, the stirred solution was transferred into a 30 cm^3 Telfon-lined stainless steel autoclave. The autoclave was sealed and put into an electric oven at 180°C for 5 h. After the hydrothermal treatment, the produced samples were collected by filtration and washed with DI water. The $LiMn_2O_4$/CNT samples were finally dried at 100°C for 12 h for further characterization. For comparative purposes, pure $LiMn_2O_4$ was prepared by a sol-gel method [21].

2.2. Material characterization

Phase purity of the materials were ascertained using powder x-ray diffractometer (XRD, Shimadzu X-ray diffractormeter 6000, Cu Kα radiation) with a scan rate of 2° min^{-1}. Morphologies of acid-treated CNTs, sol-gel prepared $LiMn_2O_4$ and $LiMn_2O_4$/CNT nanocomposite were characterized by field emission scanning electron microscopy (FESEM, Hitachi S4300). The morphology and structure of $LiMn_2O_4$/CNT nanocomposite were further investigated by transmission electron microscopy (TEM) and high resolution transmission electron microscopy (HRTEM, JEOL, JEM-2010). The mass content of CNTs in the nanocomposite was quantified using thermogravimetric analysis (TGA, Shimadzu DTG-60H).

2.3. Electrochemical measurements

The electrochemical measurements were carried out on Swagelok-type cells using Neware battery system. The positive electrode was prepared by coating a slurry, composed of 90 wt% of the $LiMn_2O_4$/CNT nanocomposite and 10 wt% of polyvinylidene difluoride (PVDF) dissolved in N-methylpyrrolidone (NMP), on an aluminum foil and dried in vacuum oven for 12h. As formed electrodes were then pressed at a pressure of 2 MPa and further dried at 100°C for another 12 h. Similar procedure was adopted to prepare the sol-gel prepared $LiMn_2O_4$ positive electrode, except for that the slurry contained 70 wt% $LiMn_2O_4$, 20% carbon black and 10 wt% PVDF. For both $LiMn_2O_4$/CNT and $LiMn_2O_4$ electrodes, the electrode thickness is about 50 μm. The electrode densities of $LiMn_2O_4$/CNT and $LiMn_2O_4$ are measured to be 2.2 and 2.6 g cm^{-3}, respectively. 1 M $LiPF_6$ in ethylene carbonate and diethyl carbonate (EC/DEC, v/v = 1:1) solution was used as the electrolyte, and lithium foil was used as both the counter and the reference electrode. Galvanostatic charge and discharge measurements were carried out in the voltage range between 3.0 and 4.5 V at different C rates (1C is 148 mA g^{-1} for $LiMn_2O_4$).

3. Results and discussion

XRD patterns of the pristine CNTs, the $LiMn_2O_4$/CNT nanocomposite, and the sol-gel prepared $LiMn_2O_4$ are shown in Fig. 1. The XRD pattern of the sol-gel prepared $LiMn_2O_4$ can be indexed to a pure spinel phase (space group Fd3m, JCPDS No. 35-0782). The diffraction peaks are strong and sharp, indicating highly crystalline feature of the sol-gel prepared $LiMn_2O_4$. The XRD pattern of the CNTs shows the typical graphite (002) and (100) reflections at 2θ values of 26.2° and 43.6°, respectively. All the diffraction peaks of the $LiMn_2O_4$/CNT nanocomposite could be indexed to the spinel $LiMn_2O_4$, except for one peak at 26.2° which could be attributed to the CNT. No diffraction peaks corresponding to impurity phase such as MnO_2 can be observed from the XRD pattern of the $LiMn_2O_4$/CNT nanocomposite, indicating the successful synthesis of $LiMn_2O_4$/CNT nanocomposite in the one-step hydrothermal treatment. The diffraction peaks from the $LiMn_2O_4$ phase of the XRD pattern of the $LiMn_2O_4$/CNT nanocomposite are quite broad compared with those of the sol-gel prepared $LiMn_2O_4$, indicating much smaller crystalline size of $LiMn_2O_4$ in the $LiMn_2O_4$/CNT nanocomposite. However, caution has to be exercised while quantifying the particle size using peak width, as micro-strain in such structures can also attribute to peak broadening [13].

Raman spectrum of the pristine CNTs furnished in Fig. 2 shows three Raman bands at 1577 cm^{-1} (G band), 1327 cm^{-1} (D band) and 2652 cm^{-1} (2D band). These bands originate from the Raman-active in-plane atomic displacement E2g mode, disorder-induced feature of the CNTs and the overtone of D band, respectively [22]. The Raman spectrum of the sol-gel prepared $LiMn_2O_4$ shows a strong peak at 625 cm^{-1} and a shoulder at 582 cm^{-1}. The band at 625 cm^{-1} is characteristic of $LiMn_2O_4$ spinel phase, corresponding to the symmetric Mn-O stretching mode of MnO_6 octahedral groups [23], and the shoulder located at 582 cm^{-1} is due to T2g(3) phonon modes. There are another two weak peaks located at 375

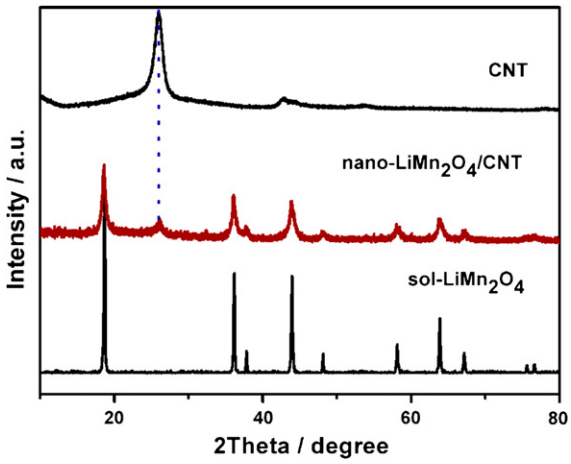

Fig. 1. XRD patterns of the pristine CNTs, the hydrothermal synthesized ultrafine $LiMn_2O_4$/CNT nanocomposite, and the sol-gel prepared $LiMn_2O_4$.

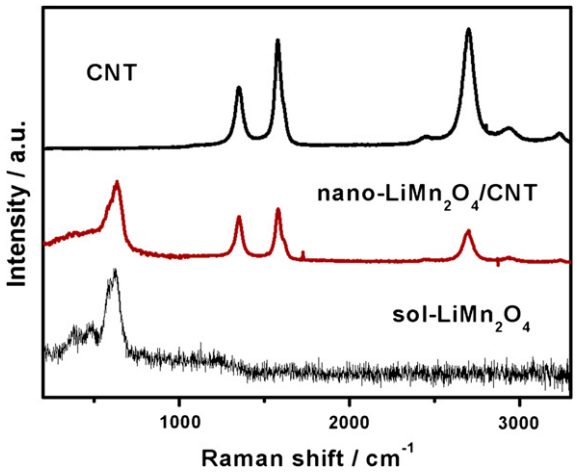

Fig. 2. Raman spectra of the pristine CNTs, the hydrothermal synthesized ultrafine $LiMn_2O_4$/CNT nanocomposite, and the sol-gel prepared $LiMn_2O_4$.

and 470 cm^{-1}, which can be assigned to T2g(1) and T2g(2) phonon modes respectively [16]. The Raman bands characteristic to CNT and to $LiMn_2O_4$ can be observed from the Raman spectrum of the $LiMn_2O_4$/CNT nanocomposite, confirming the formation of spinel $LiMn_2O_4$ phase during the hydrothermal treatment with the CNTs.

The particle size and surface morphology of the $LiMn_2O_4$/CNT nanocomposite are characterized by FESEM. The FESEM image in Fig. 3a shows that the diameter of the CNTs is in the range of 20 − 50 nm. Fig. 3b and c show the FESEM images of the $LiMn_2O_4$/CNT nanocomposite at low and high magnifications, respectively. The $LiMn_2O_4$/CNT nanocomposite exhibits a CNT matrix with $LiMn_2O_4$ nanoparticles uniformly distributed in it. Although it is difficult to ascertain the exact particle size of $LiMn_2O_4$ from Fig. 3c, it is interesting that ultrafine $LiMn_2O_4$ nanocrystallites were formed during the one-step hydrothermal synthesis. On the other hand, the particle size of the sol-gel prepared $LiMn_2O_4$ was found to be in the range from several tens to several hundreds of nanometers as shown in Fig. 3d.

To further investigate the microstructure of the $LiMn_2O_4$/CNT nanocomposite, the sample was characterized using TEM. Fig. 4a indicates that though the $LiMn_2O_4$ is not uniformly coated over the CNT's surface like MnO_2/CNT composite [24], the $LiMn_2O_4$ nanocrystallites are well mixed with the CNTs. It is important to emphasize that the CNT network can work as a separator, effectively reducing the agglomeration of $LiMn_2O_4$ nanocrystallites. Interestingly, a single CNT decorated by some $LiMn_2O_4$ nanocrystalline clusters can be observed from Fig. 4b. Fig. 4c and d show the TEM images of $LiMn_2O_4$ nanocrystallines attached on the CNT surface at different magnifications. It can be seen that the particle size of the $LiMn_2O_4$ nanocrystallites is quite uniform and mainly distributed between 10 and 20 nm. It is pertinent to note here that the addition of ethanol is critical to the formation of ultrafine $LiMn_2O_4$ nanocrystallites in the $LiMn_2O_4$/CNT nanocomposite. Without ethanol, the $LiMn_2O_4$/CNT nanocomposite can still be produced but with much larger particle size. As shown in Fig. 4d, sharp lattice fringes can be observed from the HRTEM, indicating well-crystallization of the $LiMn_2O_4$ nanoparticles. The measured interplanar spacing of 0.489 nm from the HRTEM image (Fig. 4e) corresponds to the (111) planes of $LiMn_2O_4$ [25]. Selected area electron diffraction (SEAD, Fig. 4f) reveals several diffraction rings, corresponding to $LiMn_2O_4$ (111), (311), (400), (511), (440), and CNT (002), respectively, which agree well with the XRD analysis. The content of CNTs in the $LiMn_2O_4$/CNT nanocomposite can be estimated from the TGA measurement (Fig. 5). The 20 wt% weight loss between 350 and 600°C is due to the oxidation of the CNTs in air.

To investigate the electrochemical performance of the $LiMn_2O_4$/CNT nanocomposite, galvanostatic charge/discharge experiments were conducted at 1C rate in the voltage range between 3 and 4.5 V. Fig. 6a and b show the charge/discharge curves at the first, the

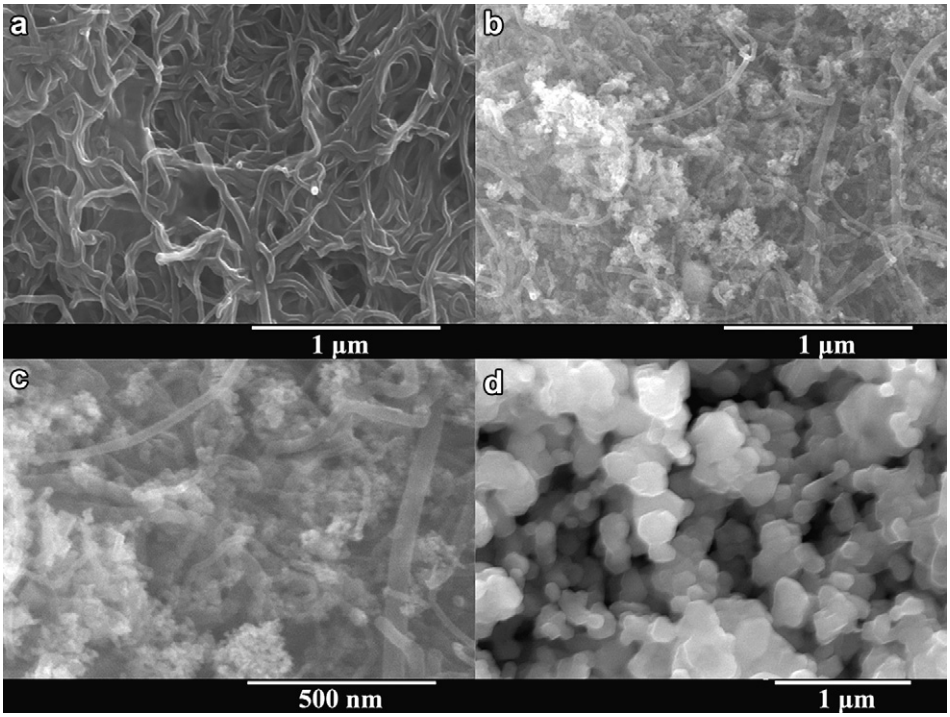

Fig. 3. (a) FESEM image of the pristine CNTs. (b) and (c) FESEM image of the hydrothermal synthesized $LiMn_2O_4$/CNT nanocomposite at low and high magnifications. (d) FESEM image of the sol-gel prepared $LiMn_2O_4$.

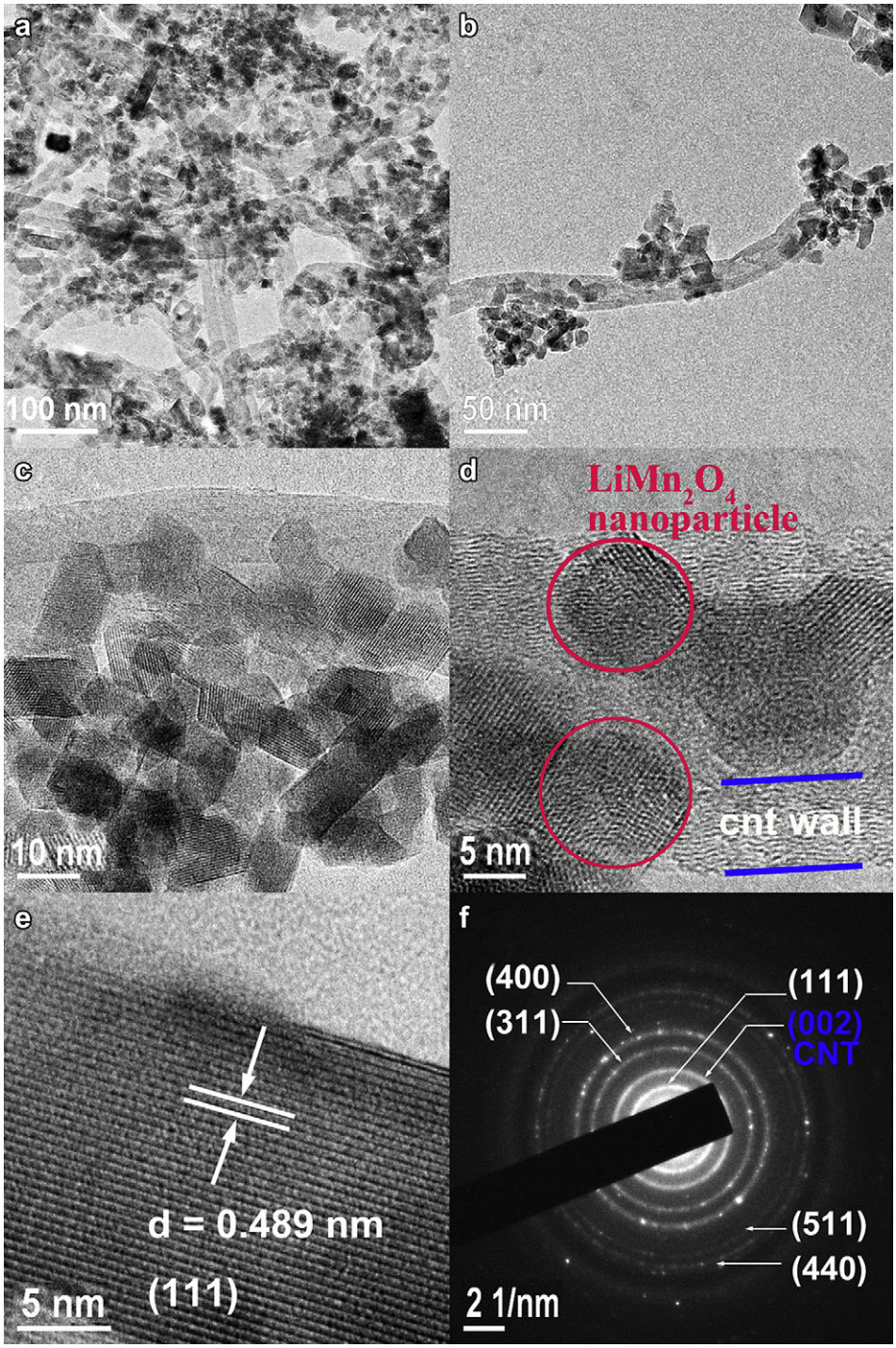

Fig. 4. (a) TEM image of the $LiMn_2O_4$/CNT nanocomposite. (b) TEM image of a single CNT decorated by $LiMn_2O_4$ nanopartcile clusters. (c and d) TEM images of $LiMn_2O_4$ nanoparticles attached on the CNT surface at different magnifications. (e) HRTEM image of one $LiMn_2O_4$ nanoparticle. (f) SEAD pattern of the $LiMn_2O_4$/CNT nanocomposite.

second and the tenth cycles for the $LiMn_2O_4$/CNT nanocomposite electrode and the sol-gel prepared $LiMn_2O_4$ electrode, respectively. Both charge and discharge curves of the $LiMn_2O_4$/CNT nanocomposite electrode exhibit two distinguished pseudoplateaus, which are ascribed to the two-phase transformation of $LiMn_2O_4$/$Li_{0.5}Mn_2O_4$, and $Li_{0.5}Mn_2O_4$/λ-MnO_2 [26]. The initial charge and discharge capacities of $LiMn_2O_4$/CNT nanocomposite electrode are 139 and 124 mAh g^{-1}, respectively, with an initial Coulombic efficiency of 89.2%. The Coulombic efficiency improves with cycling and approaches close to 100% after 10 cycles. Except for the first cycle, the charge and discharge curves of the $LiMn_2O_4$/CNT nanocomposite electrode are quite symmetrical, indicating good reversibility. In comparison, the initial charge and discharge capacities of the sol-gel prepared $LiMn_2O_4$ electrode are 109 and 79 mAh g^{-1}, respectively, with an initial coulombic efficiency of 72%. The charge and discharge curves of the sol-gel prepared $LiMn_2O_4$ electrode are not symmetrical with an obvious voltage drop at the beginning of discharge, indicating a larger electrode

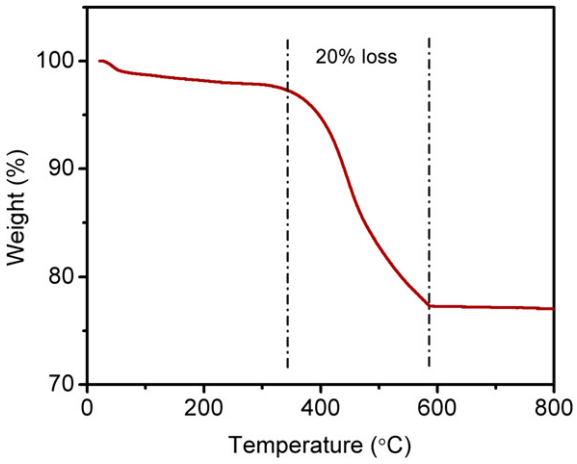

Fig. 5. TGA curve of the $LiMn_2O_4$/CNT nanocomposite.

polarization compared with the $LiMn_2O_4$/CNT nanocomposite electrode.

To evaluate the high-power capability, the $LiMn_2O_4$/CNT nanocomposite and the sol-gel prepared $LiMn_2O_4$ electrodes were cycled at different charge/discharge rates ranging from 1C to 10C. As shown in Fig. 7a, the charge curve moves to higher potential and the discharge curve moves to lower potential as the current rate increases, which is associated with the polarization of the electrode. The discharge capacities of the $LiMn_2O_4$/CNT nanocomposite electrode at 1C, 2C, 5C and 10C rates are 124, 123, 120, and 106 mAh g^{-1}, respectively. The potential separations between the charge and discharge curves of the sol-gel prepared $LiMn_2O_4$ electrode at different current rates are much larger compared with those of the $LiMn_2O_4$/CNT nanocomposite electrode, indicating a much larger polarization in the sol-gel prepared $LiMn_2O_4$ electrode. Accordingly, the discharge capacities of the sol-gel prepared $LiMn_2O_4$ electrode at 1C, 2C, 5C and 10C rates are 80 to 73, 61, and 48 mAh g^{-1}, respectively. Fig. 7c shows the charge and discharge capacities of the $LiMn_2O_4$/CNT nanocomposite electrode and the sol-gel prepared $LiMn_2O_4$ electrode at different C rates as a function of cycle number. Assuming the discharge capacity at 1C rate is the full capacity of the electrode, it can be seen that at 10C rate, the $LiMn_2O_4$/CNT nanocomposite electrode retains 85% of its full discharge capacity while the $LiMn_2O_4$ electrode only retains 60% of its full discharge capacity, indicating excellent rate capability of the $LiMn_2O_4$/CNT nanocomposite electrode. The superior electrochemical performance of the $LiMn_2O_4$/CNT nanocomposite is further demonstrated in Fig. 7d. Thus, while the nanocomposite electrode delivers discharge capacities of 116 mAh g^{-1} (92% capacity retention) after 500 cycles at 1C rate and 77 mAh g^{-1} (77% capacity retention) after 1000 cycles at 10C rate, the sol-gel prepared pristine electrode can be found to deliver a discharge capacity of only 42 mAh g^{-1} (52% capacity retention) after 200 cycles even at rates as low as 1C.

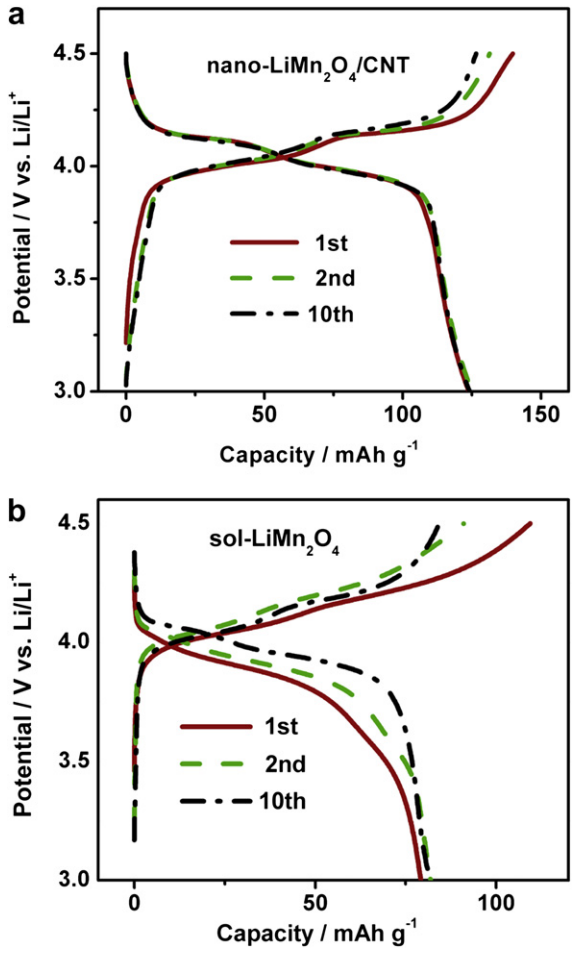

Fig. 6. (a) The 1st, 2nd, and 10th charge/discharge curves of the $LiMn_2O_4$/CNT nanocomposite electrode at 1C. (b) The 1st, 2nd, and 10th charge/discharge curves of the sol-gel prepared $LiMn_2O_4$ electrode at 1C.

The excellent rate capability and cycle performance of the $LiMn_2O_4$/CNT nanocomposite electrode could be understood from a couple of essential attributes governing its electrochemical characteristics, viz. (a) structural attribute and (b) the morphological attribute. Spinel type $LiMn_2O_4$ provides a three-dimensional pathway for ion exchange and hence each and every *hkl* plane of $LiMn_2O_4$ is capable of exchanging lithium ion with the electrolyte. The large surface area of nanocrystalline $LiMn_2O_4$ enables sufficient interfacial contact between the active material and the electrolyte, facilitating fast lithium ion transfer between the active material and the electrolyte. This holds good only for the material with a high degree of crystallinity. $LiMn_2O_4$ nanoparticles with poor crystallinity are known to possess many defects at the surface [27] which adversely affect the material's electrochemical properties [15]. More importantly, the inferior electrochemical properties of the poorly crystallized $LiMn_2O_4$ particles arise from the fact that the spinel structure may not be perfectly constructed so that not all lithium ions can be reversibly extracted and inserted. Lithium ion diffusion time within a particle is determined by the particle size ($t = L^2/D_{Li}$, where L is diffusion length) and can be drastically reduced by shifting from micrometer to nanometer particle. Hence, on the grounds of the discussions done above, the appreciable electrochemical performance of the $LiMn_2O_4$/CNT nanocomposite can be attributed to the better crystallinity of the $LiMn_2O_4$ nanocrystallites, in the composite, with uniform and small particle size (10–20 nm) guarantying very short diffusion time for the lithium ions within the $LiMn_2O_4$ particles. Furthermore, $LiMn_2O_4$ with particle size less than 15 nm can undergo lithiation/de-lithiation free from the problem of domain boundaries [28], so the lattice volume changes, during charge/discharge, in nano $LiMn_2O_4$ can occur in a more facile fashion than the bulk materials, with low mechanical stress. This provides the active material with better structural stability and hence better cycling stability. The unique morphology responsible for the observed electrochemical performance of the $LiMn_2O_4$/CNT nanocomposite can be attributed essentially to the three-dimensional conductive network formed by the highly conductive CNTs in the nanocomposite. This three-

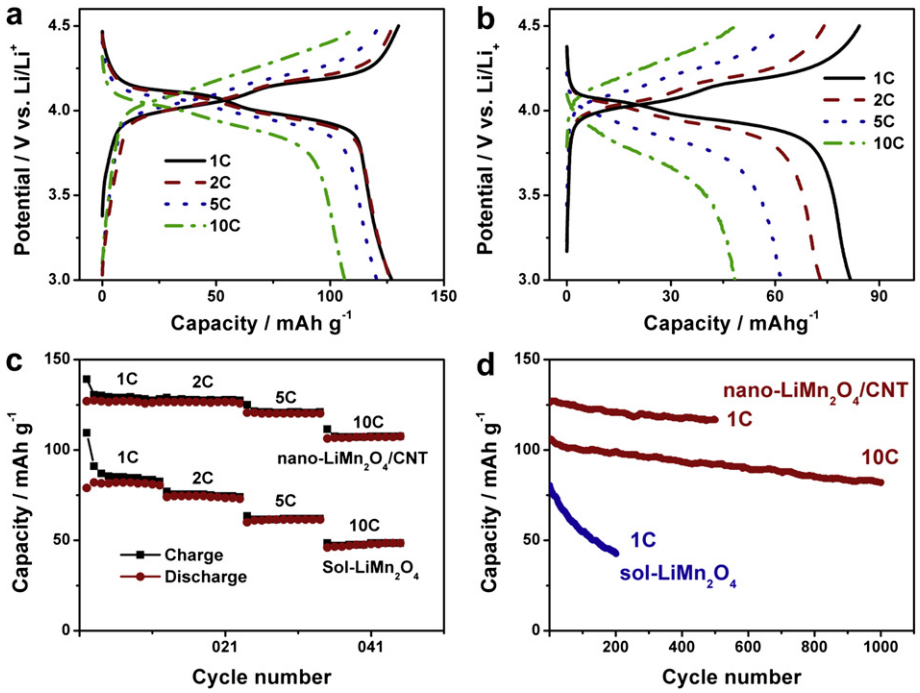

Fig. 7. (a) Charge/discharge curves of the $LiMn_2O_4$/CNT nanocomposite electrode at different C rates. (b) Charge/discharge curves of the sol-gel prepared $LiMn_2O_4$ electrode at different C rates. (c) Charge/discharge capacities of the $LiMn_2O_4$/CNT nanocomposite electrode and the sol-gel prepared $LiMn_2O_4$ electrode as a function of cycle number at different C rates. (d) Cycle performance of the $LiMn_2O_4$/CNT nanocomposite electrode and the sol-gel prepared $LiMn_2O_4$ electrode.

dimensional conductive network besides shooting up the electronic conductivity of the active material, and hence the rate capability, also controls the problem of agglomeration among the $LiMn_2O_4$ nanoparticles effectively, with only small clusters of $LiMn_2O_4$ formed in the nanocomposite. As observed from the TEM results, these small $LiMn_2O_4$ clusters are highly porous and facilitate the penetration of the electrolyte leading to an increased interfacial area between the active material and the electrolyte.

4. Conclusions

In summary, the synthesis of highly crystallized ultrafine $LiMn_2O_4$/CNT nanocomposite has been demonstrated by a one-step hydrothermal treatment using cheap reagents and with a short synthesis time of 5 h. Structural characterizations show that the material is phase pure, well crystallized, retains a spinel type structure with particle size distributed between 10 and 20 nm. The three-dimensional network formed by the carbon nanotubes provides the material with a higher electronic conductivity and also prevents agglomeration between the nanosized $LiMn_2O_4$ particles. Thus, while the sol-gel prepared $LiMn_2O_4$ could deliver a discharge capacity of only 42 mAh g^{-1} (only 52% capacity retention) after 200 cycles at rates as low as 1C, the $LiMn_2O_4$/CNT nanocomposite with unique structural and morphological features exhibits superior high-rate capability and long term cycling stability, delivering discharge capacities of 116 mAh g^{-1} (92% retention) after 500 cycles at 1C rate and 77 mAh g^{-1} (77% retention) even after 1000 cycles at rates as high as 10C, as illustrated in this paper and holds promise for applications in electric traction.

Acknowledgements

This work was supported by National Natural Science Foundation of China (Nos. 51102134 and 11134004) and Nanjing University of Science and Technology through the research grant NUST Research Funding (Nos. 2011ZDJH21 and AB41385).

References

[1] V. Etacheri, R. Marom, R. Elazari, G. Salitra, D. Aurbach, Energy Environ. Sci. 4 (2011) 3243.
[2] F.Y. Cheng, J. Liang, Z.L. Tao, J. Chen, Adv. Mater. 23 (2011) 1695.
[3] J. Hong, D.H. Seo, S.W. Kim, H. Gwon, S.T. Oh, K. Kang, J. Mater. Chem. 20 (2010) 10,179.
[4] K. Saravanan, M.V. Reddy, P. Balaya, H. Gong, B.V.R. Chowdari, J.J. Vittal, J. Mater. Chem. 19 (2009) 605.
[5] K. Saravanan, P. Balaya, M.V. Reddy, B.V.R. Chowdari, J.J. Vittal, Energy Environ. Sci. 3 (2010) 457.
[6] M.C. Yang, B. Xu, J.H. Cheng, C.J. Pan, B.J. Hwang, Y.S. Meng, Chem. Mater. 23 (2011) 2832.
[7] H.M. Wu, J.P. Tu, F.Y. Yuan, X.T. Chen, J.Y. Xiang, X.B. Zhao, G.S. Cao, J. Power Sources 161 (2006) 1260.
[8] A.R. Han, T.W. Kim, D.H. Park, S.J. Hwang, J.H. Choy, J. Phys. Chem. C 111 (2007) 11,347.
[9] T.J. Patey, R. Buchel, M. Nakayama, P. Novak, Phys. Chem. Chem. Phys. 11 (2009) 3756.
[10] H.J. Yue, X.K. Huang, D.P. Lv, Y. Yang, Electrochim. Acta 54 (2009) 5363.
[11] J.Y. Luo, H.M. Xiong, Y.Y. Xia, J. Phys. Chem. C 112 (2008) 12,051.
[12] Q.T. Qu, L.J. Fu, X.Y. Zhan, D. Samuelis, J. Maier, L. Li, S. Tian, Z.H. Li, Y.P. Wu, Energy Environ. Sci. 4 (2011) 3985.
[13] B.J. Liddl, S.M. Collins, B.M. Bartlett, Energy Environ. Sci. 3 (2010) 1339.
[14] Y. Yang, C. Xie, R. Ruffo, H. Peng, D.K. Kim, Y. Cui, Nano Lett. 9 (2009) 4109.
[15] E. Hosono, T. Kudo, I. Honma, H. Matsuda, H.S. Zhou, Nano Lett. 9 (2009) 1045.
[16] Y.L. Ding, J. Xie, G.S. Cao, T.J. Zhu, H.M. Yu, X.B. Zhao, Adv. Funct. Mater. 21 (2011) 348.
[17] F. Jiao, J.L. Bao, A.H. Hill, P.G. Bruce, Angew. Chem. Int. Ed. 47 (2008) 9711.
[18] H.W. Lee, P. Muralidharan, R. Ruffo, C.M. Mari, Y. Cui, D.K. Kim, Nano Lett. 10 (2010) 3852.
[19] X. Zhao, C.M. Hayner, H.H. Kung, J. Mater. Chem. 21 (2011) 17,297.
[20] X.L. Jia, C.Z. Yan, Z. Chen, R.R. Wang, Q. Zhang, L. Guo, F. Wei, Y.F. Lu, Chem. Commun. 47 (2011) 9669.
[21] K. Ragavendran, H.L. Chou, L. Lu, M.O. Lai, B.J. Wang, R. Ravi Kumar, S. Gopuknmar, B. Emmanuel, D. Vasudevan, D. Sherwood, Mater. Sci. Eng. B 176 (2011) 1257.
[22] X.F. Xie, L. Gao, Carbon 45 (2007) 2365.
[23] J. Proll, R. Kohler, M. Torge, S. Ulrich, C. Ziebert, M. Bruns, H.J. Seifert, W. Pfleging, Appl. Surf. Sci. 257 (2011) 9968.

[24] H. Xia, L. Lu, M.O. Lai, J. Mater. Chem. 20 (2010) 6896.
[25] F.Y. Cheng, H.B. Wang, Z.Q. Zhu, Y. Wang, T.R. Zhang, Z.L. Tao, J. Chen, Energy Environ. Sci. 4 (2011) 3668.
[26] B. Xu, Y.S. Meng, J. Power Sources 195 (2010) 4971.
[27] K. Ragavendran, V. Morchshakov, A. Veluchamy, K. Bärner, J. Phys. Chem. Solids 69 (2008) 182.
[28] M. Okubo, Y. Mizuno, H. Yamada, J. Kim, E. Hosono, H.S. Zhou, T. Kudo, I. Honma, ACS Nano 4 (2010) 741.